Available online at www.sciencedirect.com
ScienceDirect
Trans. Nonferrous Met. Soc. China 31(2021) 2323−2335
Transactions of Nonferrous Metals Society of China
www.tnmsc.cn

Microstructure and mechanical properties of TA15/TC11 graded structural material by wire arc additive manufacturing process

He WANG[1], Shu-yuan MA[1], Jia-chen WANG[2], Tao LU[1], Chang-meng LIU[1]

1. School of Mechanical Engineering, Beijing Institute of Technology, Beijing 100081, China;
2. Institute of Advanced Structure Technology, Beijing Institute of Technology, Beijing 100081, China

Received 26 August 2020; accepted 2 March 2021

Abstract: A graded structural material (GSM) with a material transition from TA15 to TC11 was fabricated by wire arc additive manufacturing (WAAM) method. The grain morphology, chemical composition, microstructure and mechanical properties of the as-deposited GSM were all characterized to investigate their variations along the deposition direction. The results indicate that from TA15 to TC11, the grain size decreases and a transition from columnar grains to equiaxed grains occurs. The content of alloy element alters greatly within a short distance, and the width of the mutation zone is 800 μm. Both TA15 and TC11 regions exhibit basketweave microstructure with α-phase and β-phase. However, during the transition from TA15 to TC11, the α-lath becomes fine, which leads to an increase in microhardness. The tensile test shows that the bonding strength at the interface is higher than the longitudinal strength of TA15, and the lateral elongation at the interface is higher than that of TA15 and TC11.

Key words: wire arc additive manufacturing; graded structural material; grain morphology; microstructure; mechanical properties

1 Introduction

The rapid development of aerospace technology has proposed high performance requirements for diversified titanium alloy structural parts due to their high specific strength and illustrious corrosion resistance [1]. In particular, there is a growing demand for graded structural material (GSM) due to its immanent advantage of microstructure and properties varing with the internal location of the component, which can optimize the overall performance of the component and achieve multifunctionality [2].

Various methods have been applied to fabricating GSM previously, such as centrifugal casting [3], self-propagating high-temperature synthesis (SHS) [4], plasma spraying [5], powder metallurgy [6] and vapor deposition [7]. However, these traditional methods usually have many limitations in practice. For example, SHS is only suitable for material system with high exothermic reactions. Vapor deposition mainly produces thin film materials, and it has low synthesis speed and high requirement for equipment. These limitations will hinder the development and application of GSM.

Compared with the above-mentioned manufacturing methods, additive manufacturing (AM) technologies have overcome fabrication challenges such as material combination, complex shape, high cost and low efficiency [8,9]. Especially, instead of traditionally coating the substrate, as a near-net shaping technology, AM can directly deposit GSM with a certain structure and shape from scratch. Therefore, AM technologies have been widely used in the direct fabrication of GSM in recent years. Additive manufacturing can be

Corresponding author: Chang-meng LIU, Tel/Fax: +86-10-68915097, E-mail: liuchangmeng@bit.edu.cn
DOI: 10.1016/S1003-6326(21)65657-1
1003-6326/© 2021 The Nonferrous Metals Society of China. Published by Elsevier Ltd & Science Press

divided into laser additive manufacturing (LAM), electron beam additive manufacturing (EBAM) and wire arc additive manufacturing (WAAM). LAM has the shortcomings of small forming size, low forming efficiency, and difficult equipment maintenance. As for EBAM, the required vacuum environment limits the working space, and it has low operability and high cost. So, LAM and EBAM can only be used to fabricate small-sized graded structural parts. Compared with LAM and EBAM, WAAM has lower production cost, stronger operability, higher deposition efficiency and material utilization, which is more suitable for rapid prototyping of large-scale graded structural parts [10,11]. In addition, the WAAM produces more stable molten pool and less spatter of molten droplet than LAM during the deposition process, which is beneficial for the preparation of GSM requiring accurate composition gradient [12].

In fact, many studies have been conducted on the fabrication of graded materials through additive manufacturing. It has been reported that many Ti-based graded structural materials were successfully fabricated by laser melting deposition. QIAN et al [13] and REN et al [14] prepared TA2/TA15 and TC4/TC11 graded materials respectively by LAM process, and made a systematic analysis on their microstructure and mechanical properties. For TC4/TC11 GSM, the effects of heat treatment and number of transition layer on microstructure and mechanical properties were also analyzed by HE et al [15]. ZHANG et al [16] fabricated functionally graded Ti−Si−N ceramic coatings with three different Ti−Si ratios (Ti, Ti−10%Si and Ti−25%Si) on commercially pure titanium substrate via laser engineering net shaping (LENS). In addition, the microstructural evolution and mechanical properties of Ti6Al4V/Rene88DT alloy, TA15/Ti2AlNb alloy and TC11/Ti2AlNb alloy manufactured by LAM were studied by LIN et al [17], LIU and ZHANG [18], and ZHANG et al [19], respectively.

However, there are few reports on fabricating GSM through WAAM. The analysis of the microstructure and properties of TA15/TC11 GSM is also rare. Recently, WANG et al [20] applied WAAM to fabricate a Ti−Al graded material with suitable mechanical properties and acceptable oxidation behavior. MARINELLI et al [21] deposited a refractory metal Ta−Mo−W GSM with linear gradient composition and hardness through WAAM. These studies show the potential of using WAAM to obtain GSM with controlled properties.

The objective of this study is to fabricate TA15/TC11 graded material by WAAM method. TA15, namely Ti−6.5Al−2Zr−1Mo−1V, is an intermediate-strength near-α titanium alloy with a β-transition temperature of 980−985 °C, whose main strengthening mechanism is solid solution strengthening of α-stabilized element Al. TC11, namely Ti−6.5Al−3.5Mo−1.5Zr−0.3Si, is a high-strength $\alpha+\beta$ dual-phase titanium alloy with a β-transition temperature of 1010 °C, which can be strengthened by heat treatment and work stably below 500 °C for a long time. As the component materials of the GSM, TA15 and TC11 are titanium alloys that are widely used in the aerospace industry. Ti-based GSM with a transition from TA15 to TC11 is expected to have promising strength and hardness. In this work, the WAAM process about this double-titanium graded alloy is firstly described. The grain morphology, chemical composition, microstructure, microhardness and tensile properties are studied to reveal their variations from TA15 to TC11, which is necessary for the design and application of the GSM.

2 Experimental

In this experiment, TA15 and TC11 were used as raw materials. The actual chemical compositions of the two wires (1.6 mm in diameter) are shown in Table 1. The schematic of the WAAM equipment used in this work is shown in Fig. 1(a). The real appearance of the equipment is shown in Fig. 1(b). The wire feeding device of the equipment is shown in Fig. 1(c). The WAAM equipment consists of four wire feeders, a gas tungsten arc welding (GTAW) equipment, a three-axis CNC machine tool, a control system and four resistance power sources. During the actual deposition process, only two wire feeders were used. As shown in Fig. 1(a), $2^{\#}$ and $3^{\#}$ wire feeders convey TA15 and TC11 wires, respectively. At first, the TA15 wire was deposited on a titanium substrate to a height of 16 layers. Subsequently, the TC11 wire was deposited on the as-deposited TA15 up to a total height of 70 mm. The deposition path and manufacturing parameters are shown in Fig. 2(a) and Table 2, respectively.

Table 1 Actual chemical compositions of two wires (wt.%)

Wire	Al	Zr	Mo	V	Si	Fe	C	O	N	H	Ti
TA15	6.69	2.14	1.65	2.11	0.022	0.026	0.039	0.12	0.02	0.0031	Bal.
TC11	6.42	1.81	3.24	0	0.3	0.034	0.013	0.085	0.021	0.01	Bal.

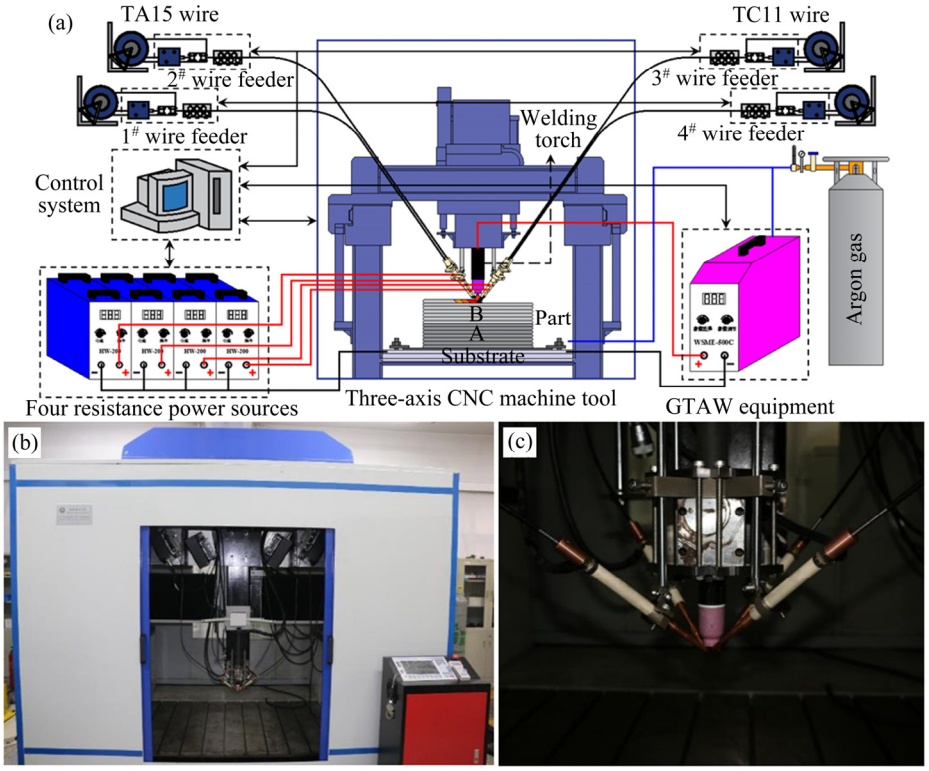

Fig. 1 WAAM equipment: (a) Schematic diagram; (b) Real appearance; (c) Device with four wire feeding nozzles

The fabricated cuboid graded part is shown in Fig. 2(b), and the position marked by red line is the bonding interface between TA15 and TC11. The block part was subjected to solution treatment at 970 °C for 1 h followed by air cooling and subsequent aging treatment at 530 °C for 6 h followed by air cooling.

For the metallographic observation, a metallographic specimen with sizes of 10 mm × 10 mm × 50 mm was cut out from the part (Fig. 2(c)). The polished longitudinal surface of the specimen was immediately etched by a mixed aqueous solution of 3 vol.% HF and 6 vol.% HNO_3 until the grain morphology appeared. The grain morphology and microstructure were observed by the optical microscope (OM) and scanning electron microscope (SEM), respectively. The main alloying elements were measured by the electron probe micro-analyzer (EPMA) to clarify the variation of chemical composition along the deposition direction. The microhardness was measured along the longitudinal surface of metallographic specimen by using a YS−38 Vickers tester with a load of 50 g for 10 s. In addition, tensile test was performed at room temperature with an Instron 5966 electronic universal material testing machine at a strain rate of 0.001 s^{-1}. There are four groups of tensile specimens need to be tested. Each group contains three samples to average. The extraction positions of four groups of tensile specimens are shown in Fig. 2(c). Group 1, labeled as GSM-L and centered at the interface of TA15 and TC11, contains three longitudinal tensile specimens which are tested to evaluate the bonding strength of two materials. Groups 2, 3 and 4, accordingly labeled as TC11-T, GSM-T and TA15-T, are cut from the TC11 region, TA15/TC11 interface region and TA15 region, respectively. These three groups are all transverse tensile specimens, on which tensile test was conducted to compare the transverse tensile properties of the TA15 region, the TA15/TC11 gradient region and the TC11 region. Figure 2(d) shows the geometrical sizes of tensile specimen.

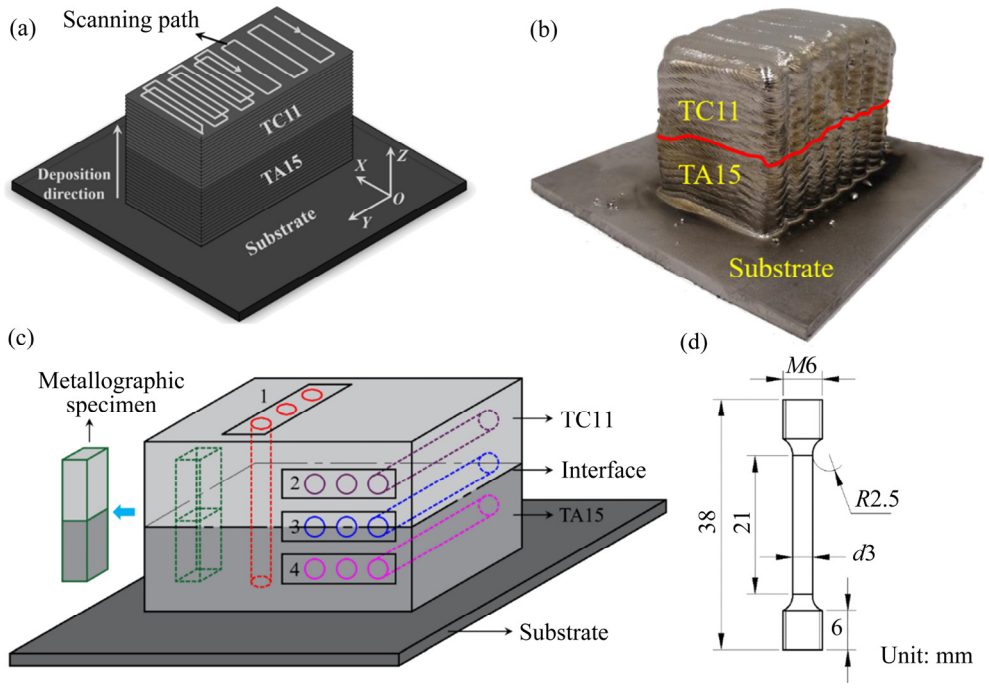

Fig. 2 TA15/TC11 GSM: (a) Deposition path; (b) Fabricated block part; (c) Extraction positions of metallographic specimen and tensile specimen; (d) Geometrical sizes of tensile specimen

Table 2 Manufacturing parameters of WAAM

Region	Average current/A	Average voltage/V	Hot-wire current/A	Layer thickness/mm	Wire feeding speed/(cm·min^{-1})	Machine scanning speed/(mm·min^{-1})
TA15	138	13.5	140	2	200	300
TC11	143	13.2	140	2.1	200	300

3 Results and discussion

3.1 Grain morphology

Figure 3 shows the grain morphology of GSM along the building direction. With the layer-by-layer transition from TA15 to TC11, the grain morphology undergoes a significant columnar-to-equiaxed transition (CET). The TA15 region is distributed with coarse columnar grains, which grow epitaxially along the deposition direction and penetrate multiple deposition layers. The graded region is dominated by fine columnar grains interspersed with equiaxed grains. In the TC11 region, the grains are basically equiaxed.

To further observe the shape and size of the grains in each area, points *a*, *b*, *c* and *d* in Fig. 3 are selected to reflect the TA15 region, the TA15/TC11 interface region, the graded region and the TC11 region, respectively. Figure 4 shows the OM images of the grain morphology corresponding to these four regions. As shown in Figs. 4(a) and (c), the columnar grains in the TA15 region have an average width of 1000 μm and consistent orientation parallel to the deposition direction, which is mainly caused by the large temperature gradient when TA15 is first deposited on the cold substrate. The grains nucleate on the substrate and compete for growth in multiple directions. However,

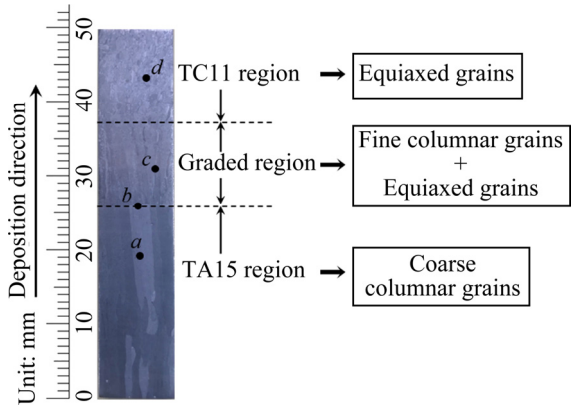

Fig. 3 Grain morphology of GSM

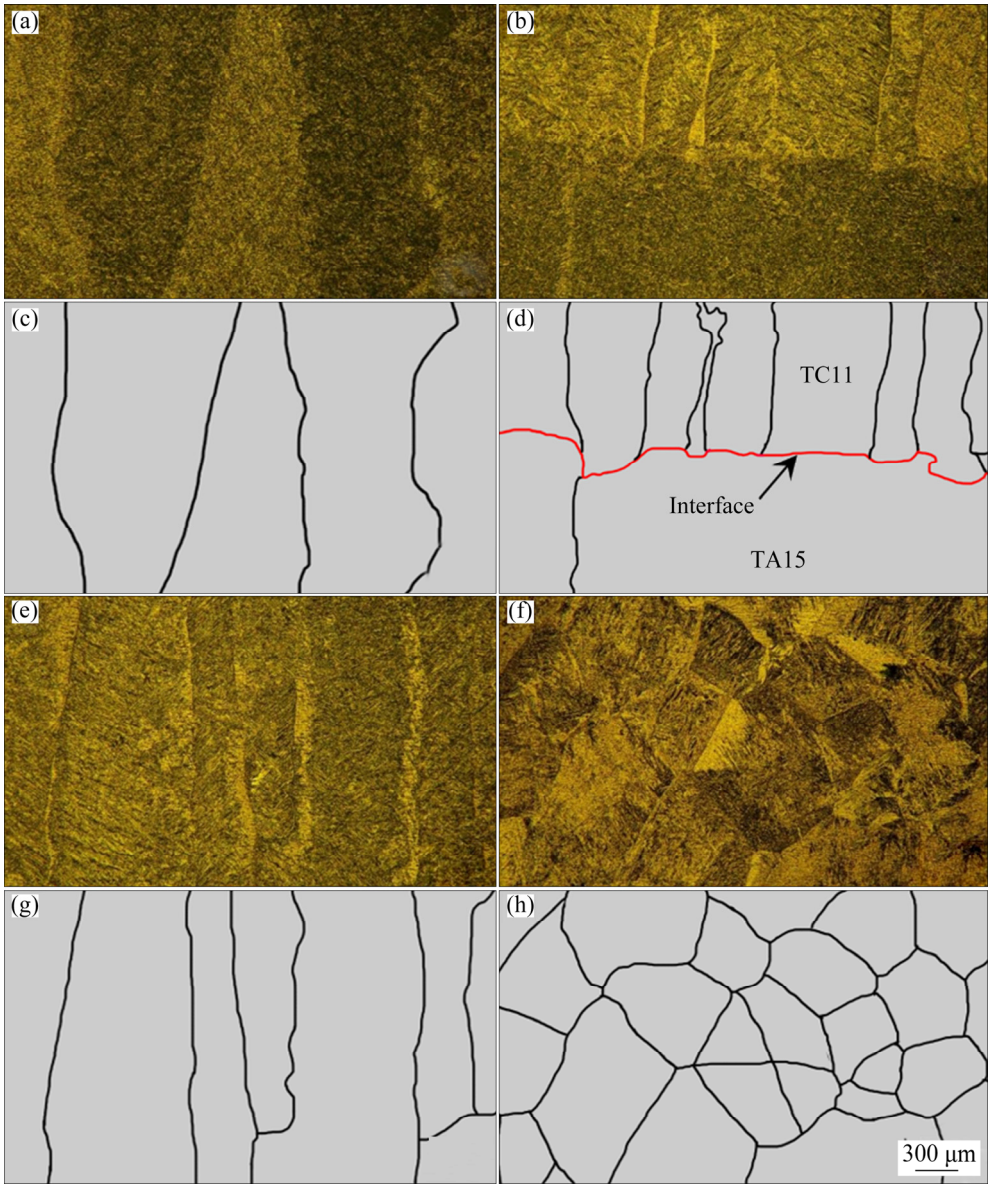

Fig. 4 Partially enlarged OM images of grain morphology (a, b, e, f) and corresponding grain boundaries outlined with black lines (c, d, g, h): (a,c) TA15 region; (b, d) TA15/TC11 interface region; (e, g) Graded region; (f, h) TC11 region

the temperature gradient perpendicular to the substrate is the largest, so the grains that grow perpendicular to the substrate dominate the competition mechanism. The large temperature gradient drives the strong epitaxial growth of the columnar grains until the deposition of TA15 ends [22]. Due to the existence of lots of heterogeneous nucleation sites on the upper surface of as-deposited TA15 part when the TC11 starts to deposit, many new columnar grains are generated, which interrupts the growth trend of pre-existing columnar grains in the TA15 region. Therefore, the columnar grains above the interface in Figs. 4(b) and (d) are finer, with an average width of 556 μm. As shown in Figs. 4(e) and (g), the average width of columnar grains (approximately 715 μm) in the graded region is slightly larger than that of the grains nucleated at the interface, which can be attributed to the heat accumulation and lack of heterogeneous nucleation sites in the melt [23]. Thermal cycling decreases the temperature gradient, which reduces the driving force for the epitaxial growth of columnar grains [22,23], so the columnar grains are shorter in the graded region. Figures 4(f) and (h) show many equiaxed grains with an average size of 543 μm and an average aspect ratio of 1.27 in pure TC11 region. In addition to the lower temperature gradient, the distribution of equiaxed

grains in the TC11 region is more attributable to the alloy elements of the TC11.

Compared with TA15, TC11 has a higher content of Mo and Si that are more conducive to the formation of equiaxed grains [24]. It is widely accepted that grain refinement is closely related to the alloy solute element that is prone to the constitutional undercooling. The constitutional undercooling will cause strong segregation at the forefront of the solid−liquid interface, which easily breaks the continuous growth of columnar grains and promotes rapid nucleation of plenty of equiaxed grains [25,26]. The relative contribution of a solute element to constitutional undercooling can be assessed by growth restriction factor Q, given by $Q=m_1c_0(k-1)$, where m_1 is the slope of the liquidus, c_0 is the solute concentration in a binary alloy, and k is the partition coefficient. As mentioned earlier, TA15 and TC11 contain five alloy elements: Al, Zr, Mo, V, and Si. Table 3 shows the growth restriction factors of these five elements in titanium calculated from the binary phase diagram information [24]. Due to the larger Q value of Mo and Si among these five elements, TC11 part is more prone to constitutional undercooling during solidification. Therefore, the grains in the TC11 area are finer and equiaxed.

Table 3 Parameters for calculation of growth restriction factor Q of binary titanium alloy

Element	m_1	k	Maximum concentration/wt.%	$m_1(k-1)$
Al	−1.7	→1	20	→0
Zr	−2.3	→1	55	→0
V	−2	→1	12	→0
Mo	6.5	2	30	6.5
Si	−28	0.333	4	18.7

(To calculate Q for a binary TiX alloy, multiply $m_1(k-1)$ by the solute concentration of element X. If c_0 is 1 wt.%, then $Q=m_1(k-1)$)

3.2 Chemical composition

The mass fractions of the main alloy elements Al, Mo, V, Zr and Si were measured by EPMA in the gradient region. As shown in Fig. 5, the chemical composition is a function of distance to a point that is 1−2 mm away from the interface and is located in the TA15 area. As expected, with the increase of distance, the contents of elements Al and Zr decrease slightly, V content decreases sharply, Mo content increases a lot, and Si content increases from zero to a lower value. Due to the existence of Ti−V multiplets, the measured V content in the TA15 region is higher than its theoretical value of 2.11 wt.%, and the V content in TC11 region is maintained at 0.4−0.5 wt.% instead of zero. According to the curves in Fig. 5, the composition transition can be divided into 5 layers, marked as A−E. The microstructure of each layer will be discussed later. It is clear that the element content only changes abruptly in the C layer with a width of 800 μm, illustrating that the interface is located in the C layer. The interface induces the composition segregation during the crystallization of C layer, resulting in uneven distribution of the alloy elements [14]. Unconspicuous compositional variation in other layers is related to the solute diffusion caused by solution and aging treatment, which can homogenize the elemental distribution of the same material layer other than the layer containing the interface between dissimilar materials [27].

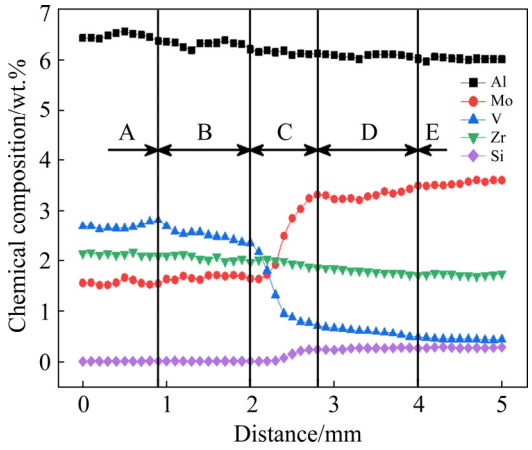

Fig. 5 Variation of chemical composition measured by EPMA

3.3 Microstructure

The OM images about the microstructures of the TA15 region, the interface transition region, and the TC11 region are presented in Fig. 6. Figure 6 indicates that TA15 and TC11 both belong to a $\alpha+\beta$ two-phase microstructure with α-laths precipitated from β-matrix, which exhibits basketweave texture integrally and Widmanstätten pattern locally. However, the difference in alloy elements of these two alloys leads to a slight difference in microstructure. As shown in Fig. 6(b), the α-lath on the TC11 side is significantly finer than that on

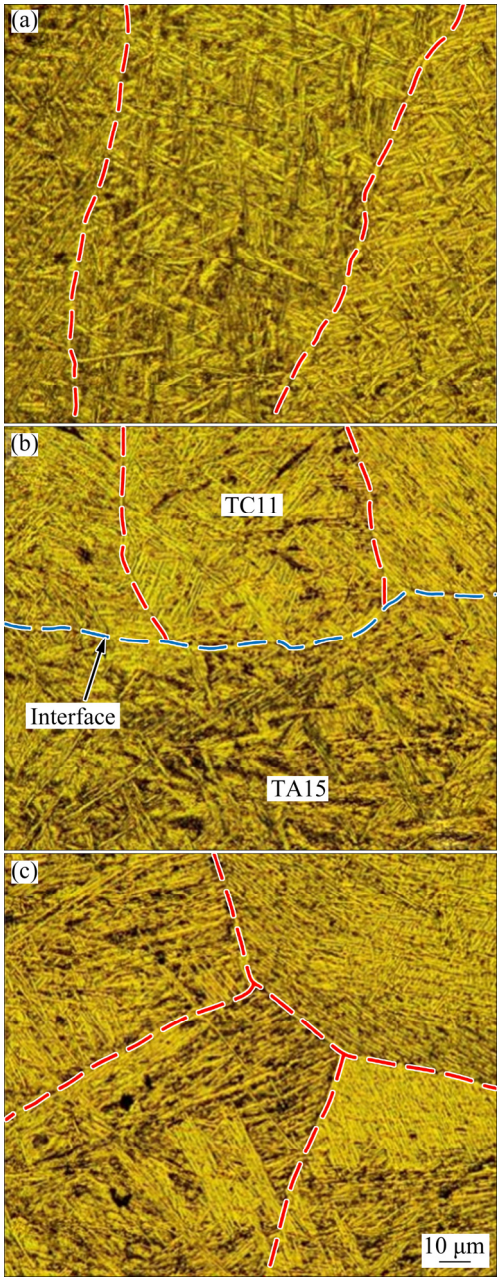

Fig. 6 OM images of microstructure: (a) TA15 region; (b) Interface transition region; (c) TC11 region

the TA15 side. The orientation of α-laths is random, and most of α-laths nucleating at the grain boundaries grow along the direction nearly perpendicular to the grain boundaries.

The microstructural evolution as a function of composition is depicted by using a series of SEM images shown in Fig. 7. In these SEM images, the black one is α-phase and the white one is β-phase. Figure 7 displays the microstructure of A layer corresponding to an average composition of Ti−6.47Al−1.57Mo−2.13Zr−2.69V−0.01Si. The microstructure consists of criss-cross primary α-laths with an average thickness of 3.3 μm and a small amount of β-phase scattered at the interface between adjacent α-laths. Figure 7(b) presents the microstructure of B layer whose average composition is Ti−6.30Al−1.68Mo−2.05Zr−2.51V−0.01Si. Compared with α-laths of A layer, α-laths of B layer are shorter, and the variation of thickness is not obvious. Figures 7(a) and (b) basically reflect the annealed microstructure of TA15 (Ti−6.5Al−2Zr−1Mo−1V). Figure 7(c) shows the microstructure of C layer corresponding to an average composition of Ti−6.14Al−2.43Mo−1.96Zr−1.18V−0.12Si. To this layer, the α-laths are significantly longer and finer. The average width of α-laths is 2.1 μm in C layer. Due to the initial deposition of TC11 wire, more β-phase exists in this layer. The microstructure of D layer is shown in Fig. 7(d). The average local composition of D layer is Ti−6.08Al−3.33Mo−1.78Zr−0.59V−0.25Si. Many α-laths that nucleate and grow at the grain boundaries (GB) are parallel to each other, forming Widmanstätten α-colonies. Since finer α-laths result in more α-phase boundaries, β-phase occupies a higher volume fraction. For E layer with an average composition of Ti−6.02Al−3.56Mo−1.72Zr−0.44V−0.28Si, the microstructure (Fig. 7(e)) belongs to basketweave structure composed of α-phases with different orientations, and more secondary α precipitates along a direction perpendicular to the boundary of the primary α. In this layer, α-laths are still fine and long, with an average thickness of 2.3 μm. Figure 7(f) illustrates the microstructure of TC11 (Ti−6.5Al−3.5Mo−1.5Zr−0.3Si) region far from the graded region. Obviously, the α-laths of TC11 are finer and shorter, and some are almost equiaxed α.

As the interface between TA15 and TC11 located in the C layer provides many nucleation sites for the lamellar α, α-laths cannot fully precipitate and grow up from the β-phase in the competitive growth mechanism. More residual β-phase is retained at the boundaries of α-laths. Consequently, the C layer is distributed with finer α-laths and more β-phase exist than other layers. In addition, from TA15 to TC11, the increase of β-stabilizing element Mo effectively inhibits the nucleation of α-phase, the decrease of α-stabilizing element Al and Zr weakens the enrichment capacity of α-phase [28]. Therefore, α-laths cannot thicken sufficiently and more β-phase remains between

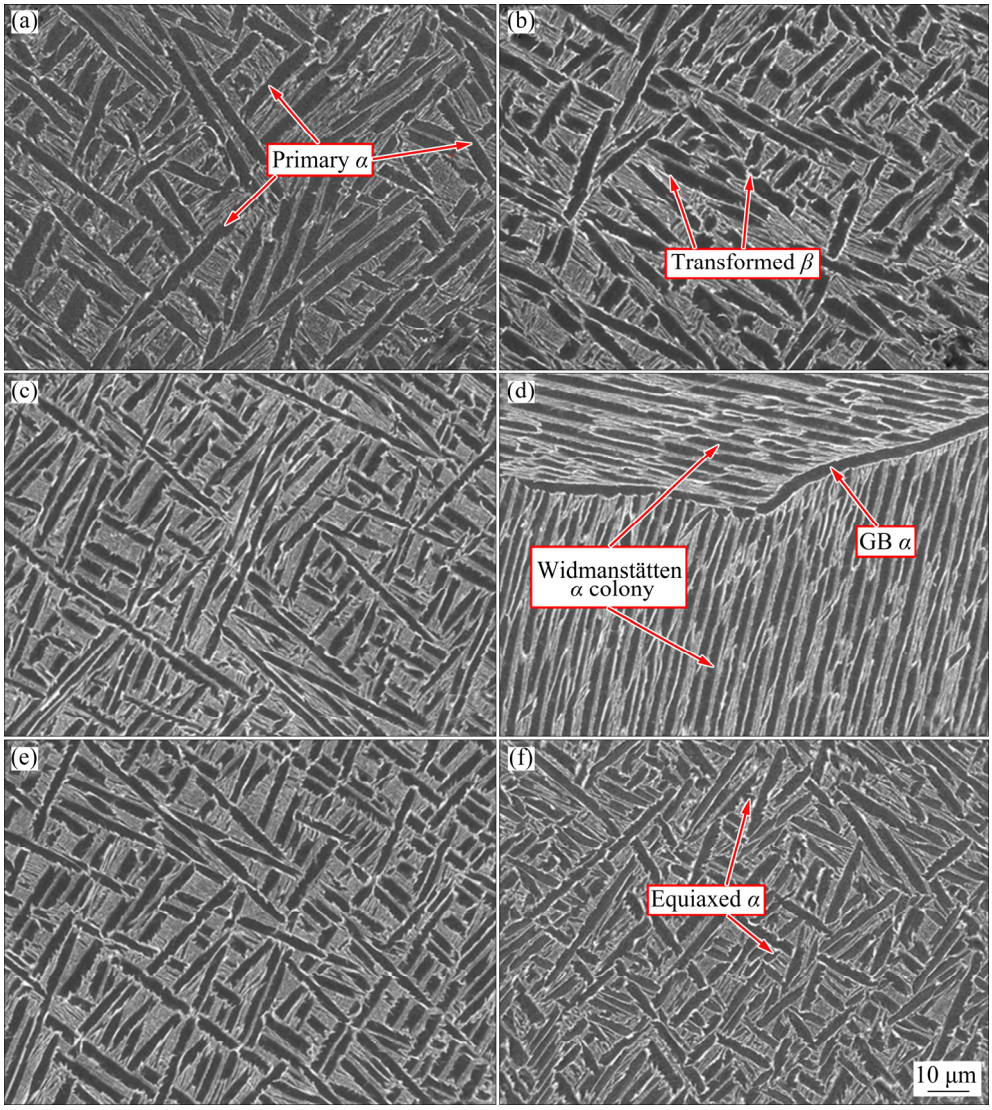

Fig. 7 Evolution of microstructure of GSM along gradient direction: (a) A layer; (b) B layer; (c) C layer; (d) D layer; (e) E layer; (f) TC11 region

adjacent α-laths. On the other hand, as TC11 has higher β-transition temperature than TA15, the α-phase in TC11 will nucleate at a higher temperature, which makes α-phase precipitate in more sites at a faster cooling rate [14]. Therefore, the α-laths of TC11 are finer.

3.4 Mcrohardness

The variation of microhardness of graded region is shown in Fig. 8. From TA15 to TC11, the microhardness increases from about HV 327 (in TA15) to HV 397 (in TC11). The increase of microhardness origins from the following two reasons. Firstly, solute elements Mo and Si increase with the deposition of TC11. Element Mo can improve the strength while Si can enhance the creep resistance, which can induce hardening to some extent [29]. Secondly, from TA15 to TC11, the

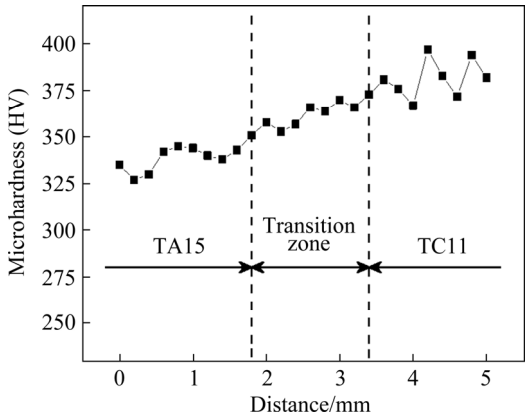

Fig. 8 Variation of microhardness along gradient direction

refined secondary α-laths and narrowed primary α-laths generate more α/β phase interfaces, which hinder the dislocation slip of grains and raise the deformation resistance [14,30].

3.5 Tensile properties

Table 4 displays tensile properties of GSM at room temperature. The data in Table 4 indicate that the room temperature tensile properties of GSM basically meet the minimum tensile property index of TA15 forgings, which proves that the performance of GSM produced by WAAM can be comparable to that of forged materials [31]. The data of EDS analysis in Table 5 show that the chemical composition of GSM-L fracture is consistent with TA15-T fracture instead of TC11-T fracture, which indicates that the GSM-L specimen breaks on the TA15 side. The actual fracture positions of three GSM-L specimens are shown in Fig. 9. In other words, the bonding strength of interface is higher than the longitudinal tensile strength of TA15. In addition, the data in Table 4 show that the ultimate tensile strength (UTS) and yield strength (YS) of GSM-T are between TA15-T and TC11-T, but the elongation (EL) of GSM-T is higher than that of TA15-T and TC11-T.

The differences of the tensile properties of GSM at different regions and directions can be explained as follows. On one hand, from TA15 to TC11, the decrease of grain size and refinement of lamellar α structure lead to a larger dislocation density, so a higher degree of grain boundary strengthening is expected according to the Hall−Petch theory [32]. Consequently, the UTS and YS of TA15-T, GSM-T and TC11-T increase sequentially as shown in Table 4, which also explains the phenomenon that the fracture of all GSM-L specimens occurs on the weak TA15 side. On the other hand, more grain boundaries traversed by stretching direction will result in poorer ductility since the existence of grain boundaries tends to reduce elongation by providing a preferential path for damage accumulation [33]. Therefore, the elongation of the TA15-T specimen of the TA15 part is higher than that of the TC11-T specimen of the TC11 part. The GSM-L specimen is distributed with columnar grains parallel to the tensile direction. The consistent orientation of adjacent columnar grains makes the plastic slip and deformation between grain boundaries easier to transmit. Therefore, GSM-L specimen exhibits better extensibility than all transverse specimens.

One interesting finding is that the elongation of GSM-T is higher than that of TA15-T and TC11-T, which should be ascribed to the fact that the interface between dissimilar material layers can delay the formation of local necking by withstanding more plastic deformation [27,34]. The stress−strain curves in Fig. 10 demonstrate that TA15 yields earlier than TC11, but TC11 necks and fractures earlier than TA15. When the tensile load is applied to both ends of the GSM-T specimen, the shear stress is produced at the interface to maintain the coordinated deformation between TA15 and

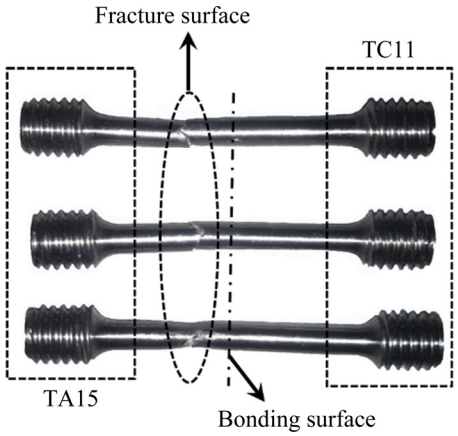

Fig. 9 Fracture positions of three GSM-L specimens

Table 4 Tensile properties of forged TA15 and deposited GSM at room temperature

Material	UTS/MPa	YS/MPa	EL/%
Wrought bar of TA15 (Q/6S 1875—2002)	930−1130	≥ 855	≥ 10
GSM-L	943±15	867±12	12.9±2.3
GSM-T	1006±21	910±18	11.2±1.1
TA15-T	985±25	887±27	10.5±0.9
TC11-T	1035±21	938±19	9.7±1.3

Table 5 EDS analysis results on fractured surface of tensile specimens (wt.%)

Material	Ti	Al	Zr	Mo	V	Si
GSM-L	86.93	6.90	2.13	1.21	2.72	0.11
TA15-T	86.99	6.76	2.18	1.36	2.63	0.08
TC11-T	86.37	6.38	1.76	4.6	0.48	0.41

TC11. After the elastic deformation stage, the TA15 part yields first and undergoes plastic deformation. The elongation of the TA15 part is higher than that of the TC11 part. For TA15 part, the shear stress acts as an additional compressive stress to retard the elongation of TA15. For TC11 part, the shear stress acts as additional tensile stress to promote TC11 to enter the yield stage. After the hardening stage, the necking firstly occurs in the TC11 part, which makes its elongation exceed that of the TA15 part. At this time, the shear stress acts as additional compressive stress inside TC11 to delay local necking, while it acts as tensile stress inside TA15 to compensate for the lack of elongation. The existence of TC11 part inhibits the propagation of internal cracks in TA15 part. Therefore, the fracture strain of GSM-T is larger than that of TA15-T.

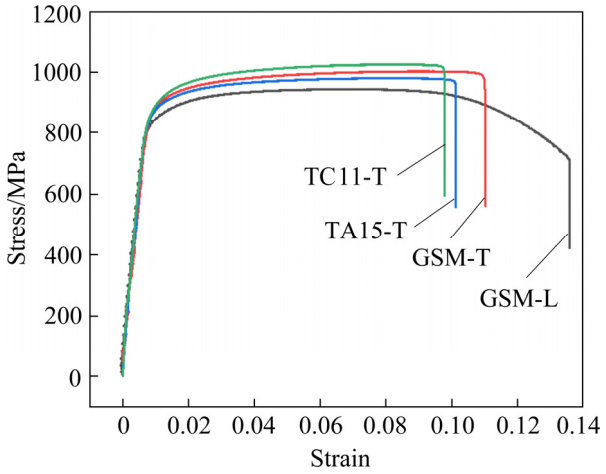

Fig. 10 Stress−strain curves of four tensile specimens

The fracture morphologies are presented in Fig. 11. Among the four groups of specimens, the fracture area of GSM-L (Fig. 11(a)) is the smallest because its highest elongation leads to the largest reduction in area. Figure 11(c) shows the overall view of the GSM-T fracture, where the distribution of two materials is clearly visible, and the red dotted line is the dividing line between TA15 and TC11. Figures 11(e) and (g) present the overall views of the TA15-T and TC11-T fractures, respectively. The ridges existing in the TC11-T fracture (Fig. 11(g)) illustrate the poor fracture toughness of TC11-T specimen. Many previous studies have verified that the large and deep dimple means ductile fracture and high elongation, but the existence of cleavage plane means near-brittle fracture and low elongation [35,36]. The dimples in Figs. 11(b) and (d) are large and deep, which is a good confirmation of the high elongation of GSM-L and GSM-T. The shallow dimples and the river-like cleavage plane can be observed in Fig. 11(f), and the fracture morphology in Fig. 11(h) is dominated by smooth cleavage plane, which is consistent with the aforementioned low elongation of TA15-T and TC11-T.

4 Conclusions

(1) The cuboid block part of TA15/TC11 GSM without surface defects is successfully fabricated by WAAM method.

(2) During the transition from TA15 to TC11, the grain size gradually decreases. The grains evolve from columnar grains to equiaxed grains due to the decreasing temperature gradient and constitutional undercooling.

(3) The chemical composition exhibits the characteristic of transient mutation due to the composition segregation at the interface. The width of mutation zone is 800 μm.

(4) The microstructure is α+β biphasic basketweave structure with Widmanstätten α-colonies mixed locally. The increase in Mo and Si content and the refined α-laths results in an increase in microhardness.

(5) The GSM-T specimen exhibits the highest elongation and centered strength in three groups of transverse specimens. The GSM-L specimen breaks on the TA15 side instead of the bonding interface, which indicates that TA15 and TC11 have obtained a high-strength metallurgical bonding at the interface. In general, TA15/TC11 GSM has acceptable strength and elongation at room temperature, which illustrates that it is feasible to fabricate the GSM via WAAM method

Acknowledgments

The authors acknowledge the financial supports from the National Natural Science Foundation of China (Nos. 51875041, 51875042). The authors are grateful to Professor Yi-nan CUI at Tsinghua University for the insightful discussion.

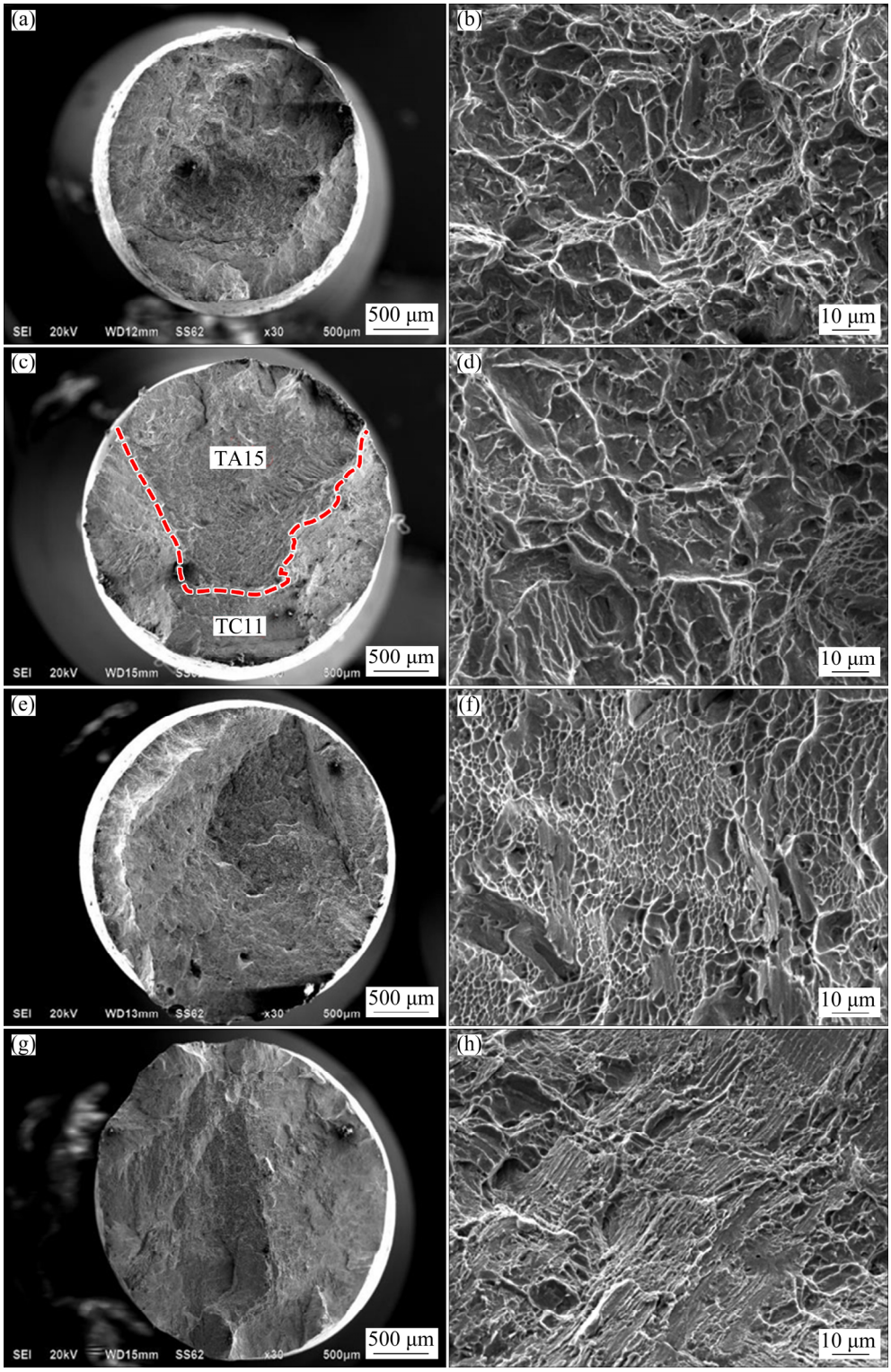

Fig. 11 SEM images of fracture morphology of GSM-L (a, b), GSM-T (c, d), TA15-T (e, f) and TC11-T (g, h): (a, c, e, g) Overall view; (b, d, f, h) High magnification

References

[1] GOMEZ-GALLEGOS A, MANDAL P, GONZALEZ D, ZUELLI N, BLACKWELL P. Studies on titanium alloys for aerospace application [J]. Defect and Diffusion Forum, 2018, 385: 419−423.

[2] NAEBE M, SHIRVANIMOGHADDAM K. Functionally graded materials: A review of fabrication and properties [J]. Applied Materials Today, 2016, 5: 223−245.

[3] MEHDITABAR A, RAHIMI G H, VAHDAT S E. Characterization of Al−Al_2Cu functionally graded material

produced by using horizontal centrifugal casting [J]. Multidipline Modeling in Materials and Structures, 2018, 14(4): 647−662.

[4] FENG G J, LI Z R, FENG S C, SHEN Z K. Effect of Ti−Al content on microstructure and mechanical properties of C-f/Al and TiAl joint by laser ignited self-propagating high-temperature synthesis [J]. Transactions of Nonferrous Metals Society of China, 2015, 25(5): 1468−1477.

[5] ZHAO Z, ZHANG S, FANG J. Preparation of functionally graded materials by plasma spraying [J]. Journal of Functional Materials, 2008, 39(2): 301−304.

[6] SZARANIEC B, GORYCZKA T. Structure and properties of Ti−Ag alloys produced by powder metallurgy [J]. Journal of Alloys and Compounds, 2017, 709: 464−472.

[7] SALIMON I A, TEMIROV A A, KUBASOV I V, SKRYLEVA E A, KISLYUK A M, TURUTIN A V, KISELEV D A, ILINA T S, ZHUKOV R N, STATNIK E S, MALINKOVICH M D, PARKHOMENKO Y N. Characterization of Si-DLC films synthesized by low cost plasma-enhanced chemical vapor deposition [J]. Materials Today: Proceedings, 2020, 33: 1997−2002.

[8] LOH G H, PEI E, HARRISON D, MONZON M D. An overview of functionally graded additive manufacturing [J]. Additive Manufacturing, 2018, 23: 34−44.

[9] LI A, LIU X, YU B, YIN B. Key factors and developmental directions with regard to metal additive manufacturing [J]. Chinese Journal of Engineering, 2019, 41(2): 159−173.

[10] WU Q R, LU J P, LIU C M, SHI X Z, MA Q, TANG S Y, FAN H L, MA S Y. Obtaining uniform deposition with variable wire feeding direction during wire-feed additive manufacturing [J]. Materials and Manufacturing Processes, 2017, 32(16): 1881−1886.

[11] DING D H, PAN Z X, CUIURI D, LI H J. Wire-feed additive manufacturing of metal components: Technologies, developments and future interests [J]. International Journal of Advanced Manufacturing Technology, 2015, 81(1−4): 465−481.

[12] SHEN C, PAN Z X, CUIURI D, ROBERTS J, LI H J. Fabrication of Fe-FeAl functionally graded material using the wire-arc additive manufacturing process [J]. Metallurgical and Materials Transactions B, 2016, 47(1): 763−772.

[13] QIAN T T, LIU D, TIAN X J, LIU C M, WANG H M. Microstructure of TA2/TA15 graded structural material by laser additive manufacturing process [J]. Transactions of Nonferrous Metals Society of China, 2014, 24(9): 2729−2736.

[14] REN H S, LIU D, TANG H B, TIAN X J, ZHU Y Y, WANG H M. Microstructure and mechanical properties of a graded structural material [J]. Materials Science and Engineering A, 2014, 611: 362−369.

[15] HE B, LIU J, YANG G. Effect of transition layers on microstructure and properties of TC4/TC11 interface fabricated by laser deposition [J]. Rare Metal Materials and Engineering, 2019, 48(3): 910−915.

[16] ZHANG Y, SAHASRABUDHE H, BANDYOPADHYAY A. Additive manufacturing of Ti−Si−N ceramic coatings on titanium [J]. Applied Surface Science, 2015, 346: 428−437.

[17] LIN X, YUE T M, YANG H O, HUANG W D. Solidification behavior and the evolution of phase in laser rapid forming of graded Ti6Al4V-Rene88DT alloy [J]. Metallurgical and Materials Transactions A, 2007, 38(1): 127−137.

[18] LIU Y, ZHANG Y. Microstructure and mechanical properties of TA15−Ti_2AlNb bimetallic structures by laser additive manufacturing [J]. Materials Science and Engineering A, 2020, 795: 140019.

[19] ZHANG Y Z, LIU Y T, ZHAO X H, TANG Y J. The interface microstructure and tensile properties of direct energy deposited TC11/Ti_2AlNb dual alloy [J]. Materials & Design, 2016, 110: 571−580.

[20] WANG J, PAN Z X, MA Y, LU Y, SHEN C, CUIURI D, LI H J. Characterization of wire arc additively manufactured titanium aluminide functionally graded material: Microstructure, mechanical properties and oxidation behaviour [J]. Materials Science and Engineering A, 2018, 734: 110−119.

[21] MARINELLI G, MARTINA F, LEWTAS H, HANCOCK D, GANGULY S, WILLIAMS S. Functionally graded structures of refractory metals by wire arc additive manufacturing [J]. Science and Technology of Welding and Joining, 2019, 24(5): 495−503.

[22] YIN J, PENG G, CHEN C, YANG J, ZHU H, KE L, WANG Z, WANG D, MA M, WANG G, ZENG X. Thermal behavior and grain growth orientation during selective laser melting of Ti−6Al−4V alloy [J]. Journal of Materials Processing Technology, 2018, 260: 57−65.

[23] WANG T, ZHU Y Y, ZHANG S Q, TANG H B, WANG H M. Grain morphology evolution behavior of titanium alloy components during laser melting deposition additive manufacturing [J]. Journal of Alloys and Compounds, 2015, 632: 505−513.

[24] BERMINGHAM M J, MCDONALD S D, DARGUSCH M S, STJOHN D H. Grain-refinement mechanisms in titanium alloys [J]. Journal of Materials Research, 2011, 23(1): 97−104.

[25] ZHU Y Y, TANG H B, LI Z, XU C, HE B. Solidification behavior and grain morphology of laser additive manufacturing titanium alloys [J]. Journal of Alloys and Compounds, 2019, 777: 712−716.

[26] BERMINGHAM M J, STJOHN D H, KRYNEN J, TEDMAN-JONES S, DARGUSCH M S. Promoting the columnar to equiaxed transition and grain refinement of titanium alloys during additive manufacturing [J]. Acta Materialia, 2019, 168: 261−274.

[27] REN H S, TIAN X J, WANG H M. Effect of heat treatment on microstructure and mechanical properties of a graded structural material [J]. Materials Science and Engineering A, 2014, 614: 207−213.

[28] SUI N, CAO J, HUANG X, GAO F, TAN Q. Effect of composition on microstructure and mechanical properties of TA15 titanium alloy [J]. Journal of Aeronautical Materials, 2019, 39(1): 48−54.

[29] LIANG Y J, TIAN X J, ZHU Y Y, LI J, WANG H M. Compositional variation and microstructural evolution in laser additive manufactured Ti/Ti−6Al−2Zr−1Mo−1V graded structural material [J]. Materials Science and Engineering A, 2014, 599: 242−246.

[30] XU W F, MA J, LUO Y X, FANG Y X. Microstructure and high-temperature mechanical properties of laser beam welded TC4/TA15 dissimilar titanium alloy joints [J]. Transactions of Nonferrous Metals Society of China, 2020, 30(1): 160−170.
[31] HUANG D M, WANG H L, CHEN X, CHEN Y, GUO H. Influence of forging process on microstructure and mechanical properties of large section Ti−6.5Al−1Mo−1V−2Zr alloy bars [J]. Transactions of Nonferrous Metals Society of China, 2013, 23(8): 2276−2282.
[32] BORODIN E N, MAYER A E. Influence of structure of grain boundaries and size distribution of grains on the yield strength at quasistatic and dynamical loading [J]. Materials Research Express, 2017, 4(8): 085040.
[33] CARROLL B E, PALMER T A, BEESE A M. Anisotropic tensile behavior of Ti−6Al−4V components fabricated with directed energy deposition additive manufacturing [J]. Acta Materialia, 2015, 87: 309−320.
[34] WANG Y F, WANG M S, YIN K, HUANG A H, LI Y S, HUANG C X. Yielding and fracture behaviors of coarse-grain/ultrafine-grain heterogeneous-structured copper with transitional interface [J]. Transactions of Nonferrous Metals Society of China, 2019, 29(3): 588−594.
[35] LI Z, LIU C, XU T, JI L, WANG D, LU J, MA S, FAN H. Reducing arc heat input and obtaining equiaxed grains by hot-wire method during arc additive manufacturing titanium alloy [J]. Materials Science and Engineering A, 2019, 742: 287−294.
[36] ZHANG T, ZHAO X, LIU J, ZHANG R, WANG X, YUAN Y, LI Z, HAN Z. The microstructure, fracture mechanism and their correlation with the mechanical properties of as-cast Mg−Nd−Zn−Zr alloy under the effect of cooling rate [J]. Materials Science and Engineering A, 2021, 801: 140382.

丝材电弧增材制造 TA15/TC11 梯度结构材料的显微组织和力学性能

王 贺[1]，马树元[1]，王嘉琛[2]，鲁 涛[1]，刘长猛[1]

1. 北京理工大学 机械与车辆学院，北京 100081；
2. 北京理工大学 先进结构技术研究院，北京 100081

摘 要：利用丝材电弧增材制造的方法制备从 TA15 过渡为 TC11 的梯度结构材料，并对该梯度结构材料的晶粒形态、化学成分、显微组织和力学性能沿沉积方向的变化情况进行表征和研究。结果表明，从 TA15 到 TC11，晶粒尺寸减小，并且发生从柱状晶到等轴晶的转变。合金元素的含量在短距离内变化很大，突变区的宽度为 800 μm。TA15 区域和 TC11 区域均呈现出 $\alpha+\beta$ 双相网篮状组织。随着从 TA15 到 TC11 的过渡，α 板条变细，这导致显微硬度的增加。拉伸试验表明，界面处的结合强度高于 TA15 部分的纵向强度，界面处的横向伸长率高于 TA15 部分和 TC11 部分的横向伸长率。

关键词：丝材电弧增材制造；梯度结构材料；晶粒形态；显微组织；力学性能

(Edited by Xiang-qun LI)